



**HAL**  
open science

## Contactless Bio-Electrofunctionalization of Planar Micropores

Abdulghani Ismail, Pascale Pham, Lucie Descamps, Ali Maziz, Emeline Descamps, Thierry Leïchlé, Patrice Marche, Thierry Livache, Camille Raillon, Yoann Roupioz, et al.

► **To cite this version:**

Abdulghani Ismail, Pascale Pham, Lucie Descamps, Ali Maziz, Emeline Descamps, et al.. Contactless Bio-Electrofunctionalization of Planar Micropores. *Advanced Materials Technologies*, 2021, 6 (6), pp.2001154. 10.1002/admt.202001154 . hal-03259683

**HAL Id: hal-03259683**

**<https://hal.science/hal-03259683v1>**

Submitted on 28 Nov 2022

**HAL** is a multi-disciplinary open access archive for the deposit and dissemination of scientific research documents, whether they are published or not. The documents may come from teaching and research institutions in France or abroad, or from public or private research centers.

L'archive ouverte pluridisciplinaire **HAL**, est destinée au dépôt et à la diffusion de documents scientifiques de niveau recherche, publiés ou non, émanant des établissements d'enseignement et de recherche français ou étrangers, des laboratoires publics ou privés.

# Contactless Bio-Electrofunctionalization of Planar Micropores

Abdulghani Ismail,\* Pascale Pham, Lucie Descamps, Ali Maziz, Emeline Descamps, Thierry Leïchlé, Patrice N. Marche, Thierry Livache, Camille Raillon, Yoann Roupioz, Pascal Mailley, Arnaud Buhot, Loïc Leroy, and Aurélie Bouchet-Spinelli\*

The localized functionalization of pores and channels of micrometric and sub-micrometric sizes is a bottleneck in surface chemistry. A method for the regioselective chemical functionalization of planar pores is presented, that are, restrictions in microfluidic channels, here made of SiO<sub>2</sub>-coated silicon. This strategy, based on bipolar electrochemistry, exploits the combined presence of the constriction and a localized deoxidation pattern within the pore that affects the electrical field distribution inside the microfluidic channel. It is not only shown that it is capable of regioselectively functionalizing a planar pore at relatively small potential difference applied across it, but also the possibility of positioning the functionalization area inside or at the edges of the pore depending on the design of the deoxidation pattern is proved. These results are in perfect correlation with the numerical simulations of electric field distribution in micropores carried out using the software Comsol Multiphysics. This functionalization technique is therefore very promising, particularly in the field of biosensors. A specific DNA hybridization test has been successfully carried out, which represents a first step toward bioanalytical and health applications.

in conductance (or resistance).<sup>[4]</sup> Usually the pore size is chosen to be slightly larger than the target molecule or cell. The synthetic solid state pores offer advantages over the biological pores in terms of better controlling the size and number of pores per unit area, as well as being more resistant to sensing conditions (pH, temperature, and ionic force) and easier to functionalize.<sup>[5]</sup> The best method to distinguish between two molecules having similar size is to functionalize the pore in a manner that the slowing down or capture of the target molecule in the pore has its own temporal imprint compared to the speed of other molecules.<sup>[6]</sup> This is usually obtained from the monitoring of the ionic current drop between the passage of target biomolecules and non-specific ones. Several functionalization methods have been developed including chemisorption of functional molecules through silanization or thiol-gold linkage,<sup>[7]</sup> deposition techniques

(chemical and physical vapour deposition,<sup>[8]</sup> electroless deposition,<sup>[9]</sup> and atomic layer deposition),<sup>[10]</sup> chemical modification of the functional group on the nanopore to yield polymer brushes<sup>[11]</sup> or hydrogels,<sup>[12]</sup> and plasma surface modification.<sup>[13]</sup> These techniques are usually based on the functionalization of the pore and of the immediately adjacent membrane surface, which leads to capture of large amounts of molecules on the

## 1. Introduction

Solid state pores, from nano- to micrometric dimensions, have been extensively used over the last decade for sensing biomolecules and cells.<sup>[1–3]</sup> After application of a DC electric field between two electrodes present at each side of the pore, the passage of biomolecules through the pore is detected by a change

Dr. A. Ismail, L. Descamps, Dr. T. Livache, Dr. C. Raillon, Dr. Y. Roupioz, Dr. A. Buhot, Dr. L. Leroy, Dr. A. Bouchet-Spinelli  
Univ. Grenoble Alpes CEA CNRS IRIG  
SyMMES  
Grenoble F-38000, France  
E-mail: abdul.ismail@manchester.ac.uk; aurelie.bouchet-spinelli@cea.fr

Dr. P. Pham, Dr. P. Mailley  
Univ. Grenoble Alpes  
CEA LETI  
Grenoble F-38000, France

Dr. A. Maziz, Dr. E. Descamps, Dr. T. Leïchlé  
LAAS-CNRS  
Université de Toulouse  
CNRS  
Toulouse, France

Dr. E. Descamps  
ToNIC  
Toulouse NeuroImaging Center  
University of Toulouse  
INSERM  
UPS  
Toulouse, France

Dr. T. Leïchlé  
School of Electrical and Computer Engineering  
GeorgiaTech-CNRS International Research Laboratory  
Atlanta, GA, USA

Dr. P. N. Marche  
U1209 INSERM  
CNRS UMR5309  
Université Grenoble-Alpes  
France

 The ORCID identification number(s) for the author(s) of this article can be found under <https://doi.org/10.1002/admt.202001154>.

DOI: 10.1002/admt.202001154

membrane before entering the pore, finally resulting in loss of sensitivity with this method.<sup>[14]</sup> Several methods have been developed that permit a localized functionalization of the pore while excluding the surrounding membrane. However, such methods are often multistep, time-consuming, and difficult to implement.<sup>[15]</sup> Since 2009, we have developed a new strategy to locally functionalize silicon/silicon oxide micro- and nanopores using polypyrrole, iridium oxide, gold nanoparticles, and metal using the “ContactLess ElectroFunctionalization (CLEF)” strategy.<sup>[16–20]</sup> This method relies on the application of a voltage between the two sides of a traversing pore drilled in a SiO<sub>2</sub>-covered silicon membrane, which allows the localized functionalization on the internal walls of the pore. Although the mechanisms underlying our CLEF method are not clearly identified, we believe that the combined effect of the pore restriction (which induces a high electric field) together with the presence of defects in the silicon oxide layer covering the pore walls is the key of this method’s success.

Micro- and nanopores are usually fabricated by drilling through a solid membrane using chemical etching,<sup>[21]</sup> ion-track etching,<sup>[22]</sup> focused ion beam,<sup>[23]</sup> helium ion beam,<sup>[24]</sup> controlled dielectric breakdown,<sup>[25]</sup> laser ablation,<sup>[26]</sup> controlled optical etching,<sup>[27]</sup> or electron beam carving.<sup>[28]</sup> These methods result in “traversing” micro- and nanopores that are not easy to couple to fluidic connections or optical readout (e.g. cell capturing), parallelization, multiplexing, etc. Restrictions with micropore geometry have been demonstrated in PDMS, glass, and silicon and used for applications similar to those of traversing micropores.<sup>[29–35]</sup> Such restrictions are hereafter referred to as “planar pores”. Planar pores are much easier to use than traversing pores and their manufacture may be easily industrialised using conventional microelectronics techniques. Recently, we have demonstrated the importance of combining microfluidics with planar micropores using bipolar electrochemistry (BPE) in order to produce light-emitting pores by electrochemiluminescence (ECL).<sup>[36]</sup> Briefly, similarly to the potential drop obtained during CLEF on 3D traversing pores, the potential drop on each side of the planar pores permitted the selective ECL emission of the planar pore. Thanks to the presence of the planar pore, the applied voltages were two orders of magnitude lower than traditional BPE setups, thus avoiding electrical arcing and air bubbles, permitting further usage of the setup for Coulter counter on micro- and nano-objects.

Herein we investigate the suitability of CLEF technology for selective biomolecule functionalization of planar micropores. Such functionalization of the pores could increase the sensing capabilities of the pores toward micrometric objects such as cells.<sup>[17,19]</sup> The etching of insulating SiO<sub>2</sub> in the micropore was a critical point for the functionalization to take place. The BPE principle inside this configuration by oxidation on one side of the pore and reduction on the other side is demonstrated in this work. Application of 10 V between two electrodes on either side of the planar micropore with a low ionic strength electrolyte was necessary for the localized electrodeposition of DNA probes coupled to pyrrole in order to form polypyrrole (PPy)-DNA combs. Revelation of the functionalization was demonstrated by fluorescence microscopy, by labelling of the complementary DNA strand, and by SEM imaging; and validated through numerical simulations of the electric field.

## 2. Results and Discussion

### 2.1. CLEF of Planar Micropores

Microfluidic chips bearing two feeder gold electrodes and a single planar micropore were fabricated to study the functionalization of silicon using CLEF (Figure 1A). The cross-sectional area of the fluidic “butterfly” channel was 400 μm × 100 μm, tapering to 10 μm × 10 μm at the pore. The purpose of the butterfly shape, which decreases in width gradually, is to guide the biomolecules to pass homogeneously through the micropore and to avoid the formation of air bubbles in the channel. The length of the pore was 20 μm. The gold feeder electrodes—each 50 μm in diameter—were separated from each other by 1.2 mm and from the highly *p*-doped silicon ( $\rho < 0.01 \Omega\cdot\text{cm}$ ) by a 300 nm layer of SiO<sub>2</sub>, obtained through dry thermal oxidation. The high-quality insulating SiO<sub>2</sub> layer was necessary to channel electron flow through only desired regions of the silicon. Deoxidation of silicon dioxide at specific regions to study the electrofunctionalization was necessary in order to force electrons through the silicon thus promoting BPE processes (Figure S2, Supporting Information).

The chips were then aligned and bonded with the PDMS, which was moulded with a pattern of two unconnected half-butterflies, similar to the pattern of the silicon chips (Figure S3, Supporting Information). Fluidic channels were punched in PDMS so as to introduce a deposition solution containing pyrrole monomers and pyrrole-ODN conjugates. The PPy functionalization was detected using fluorescence microscopy after hybridization of the complementary biotinylated and grafted ODNs, followed by interaction of the biotin with a fluorescent probe (SAPE) (Figure S4, Supporting Information).

Preliminary experiments were carried out on chips bearing a fully deoxidized “butterfly” area in order to prove the possibility of BPE processes in such a configuration (Figure 1A). Several voltages and durations were tested. The optimal parameters were found to be 10 V with a duration of 1 s. This 10 V voltage led to the electrodeposition of PPy on the positive feeder gold electrode and on the deoxidized butterfly compartment opposite the positive electrode (near the negative electrode) (Figure 1B). Longer deposition durations and voltages led to the detachment of the deposited layer from these surfaces, most likely due to overoxidation of PPy. The ionic strength of the electrolyte also showed interesting effects on the functionalization. Using high ionic strength electrolytes (such as 0.5 M KNO<sub>3</sub> or KCl) instead of low ionic force (10 mM KCl) did not permit any functionalization of silicon areas whereas the feeder electrodes were functionalized. This shows that the functionalization is dependent on the balance between the conductivities of silicon and of the electrolyte. If the electrolyte has a too large ionic strength, electron transfer through the silicon is no longer significant. Besides, using a fully oxidized silicon wafer (without deoxidation) or taking out the fluidic restriction (i.e. a simple PDMS channel without a pore) also resulted in disappearance of functionalization (data not shown). Two conclusions could be drawn from these results. First, functionalization occurs only on half of the deoxidized area, which shows that an electron transfer through the silicon is necessary for functionalization. Second, the presence of the planar micropore and the geometry

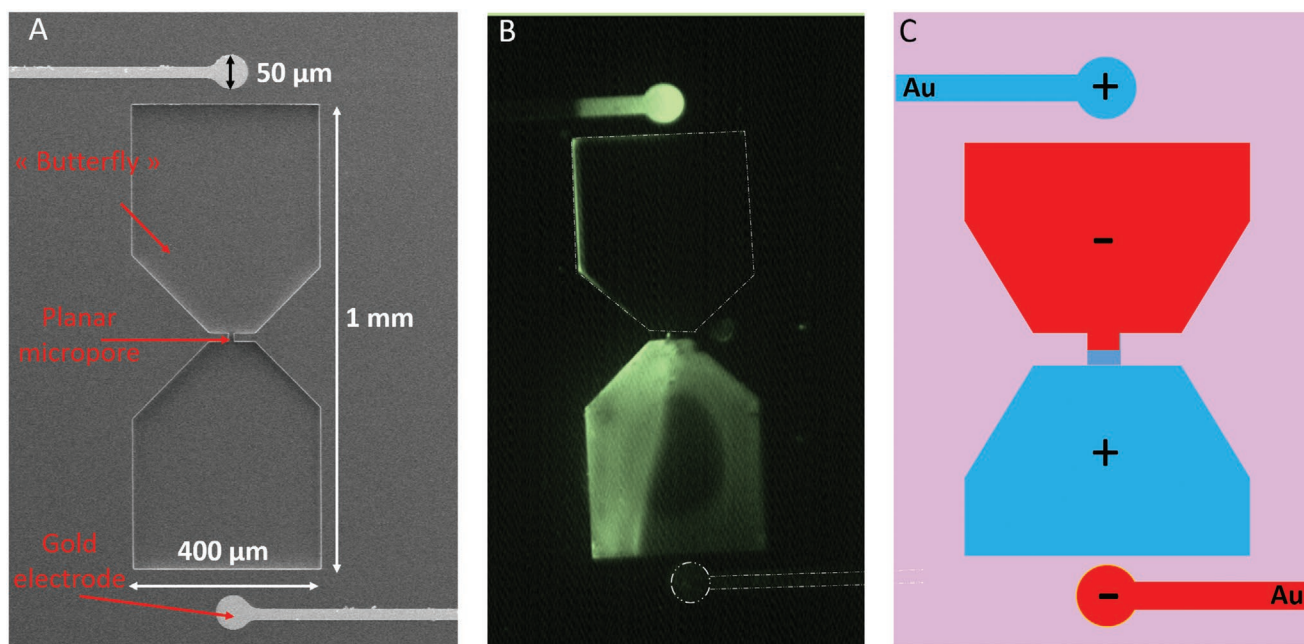


**Figure 1.** A) SEM image of the microfluidic device showing the deoxidized butterfly, the micropore, and the feeder electrodes; B) Revelation of PPy grafting using fluorescence microscopy. The hybridization of grafted DNA with its biotinylated complementary strand is revealed using SAPE. PPy was electrodeposited using 10 V for 1 s pulse between the two integrated gold electrodes after filling the microfluidic channels using pyrrole 100 mM + py-ODN 10  $\mu\text{M}$  + KCl 10 mM. Obj 10 $\times$ , exposure time 0.32 s, bining 4 $\times$ ; C) Polarization of the different parts of the chip after voltage application: blue (+) and red (-) colors (signs) refer to the cathodic or anodic behaviors on the chip in BPE.

of the chip are necessary to polarize the silicon thanks to the potential drop through the restriction.

Inversely, the electro-reduction of silver nitrate could be observed on the butterfly compartment opposite to the negative electrode (Figure S5, Supporting Information). These experiments demonstrate the bipolarization of the deoxidized “butterfly” region under the application of a voltage. As shown in Figure 1C, the application of a voltage between the two gold feeder electrodes provokes the bipolarization inside the “butterfly” area creating a virtual cathode on one side, and a virtual anode on the other.

To go a step further and apply this BPE process to the functionalization of planar micropores, the deoxidation area was reduced to approximately the size of the micropore. Indeed, two deoxidation patterns were studied (Figure 2): i) a 30  $\mu\text{m}$   $\times$  30  $\mu\text{m}$  “large” deoxidation pattern including the pore area (thus the pore full 20  $\mu\text{m}$   $\times$  20  $\mu\text{m}$  area is deoxidized including its walls) and ii) 10  $\mu\text{m}$   $\times$  30  $\mu\text{m}$  “small” deoxidation pattern inside the pore (thus a partial 10  $\mu\text{m}$   $\times$  10  $\mu\text{m}$  of the pore area is deoxidized including the pore walls).

The functionalization of each micropore using DNA-functionalized PPy and its revelation were achieved with a similar protocol than the one used in the previous experiments. The fluorescence observations of the functionalization showed, for the case of the “large” deoxidation area, that the electrodeposition of PPy occurred only on the walls of the pore, which are opposite to the anode (Figure 3A). For the case of “small” deoxidation, a localized functionalization was only observed on the deoxidized part on one side of the pore (Figure 4A). Besides, in both cases, the electrodeposition was also observed on the feeder anode. A comparison of the respective dimensions of

the fluorescent and deoxidized areas showed nice agreement (Figure S6, Supporting Information).

SEM images confirmed the results obtained in fluorescence microscopy. In the case of large deoxidation, no deposit was observed on one side of the pore (Figure 5B), which confirms the results obtained with fluorescence experiments (Figure 5A). SEM images of PPy deposits on the other side of the micropore showed its typical cauliflower structure and confirmed that it is mainly localized on the external walls of the micropore and at its bottom (Figure 5B). The deoxidation pattern cannot be a perfect square and consequently the deposit at the base seems to follow its shape. A remarkable asymmetry of PPy electrodeposition on the deoxidised walls as well as on the base of the deoxidized silicon square is observed. This asymmetry is due to the non perfect desoxidation of silicon oxide resulting from the alignment accuracy during the photolithography process when aligning the desoxidation pattern onto the previously etched pattern in silicon that constitute the microfluidic pore. This asymmetry serves here as a direct proof of the influence of the desoxidation pattern on the polypyrrole deposition area. The deposit is not localized inside the micropore in the case of large deoxidation.

## 2.2. Numerical Simulations of the Electric Field in Micropores

As we did in previous works for drilled micropores,<sup>[17]</sup> numerical simulations of the electric fields in the micropore were developed in order to better understand the potential drop and its dependence on the deoxidation pattern and the presence of a pore restriction. We showed in previous works that, without

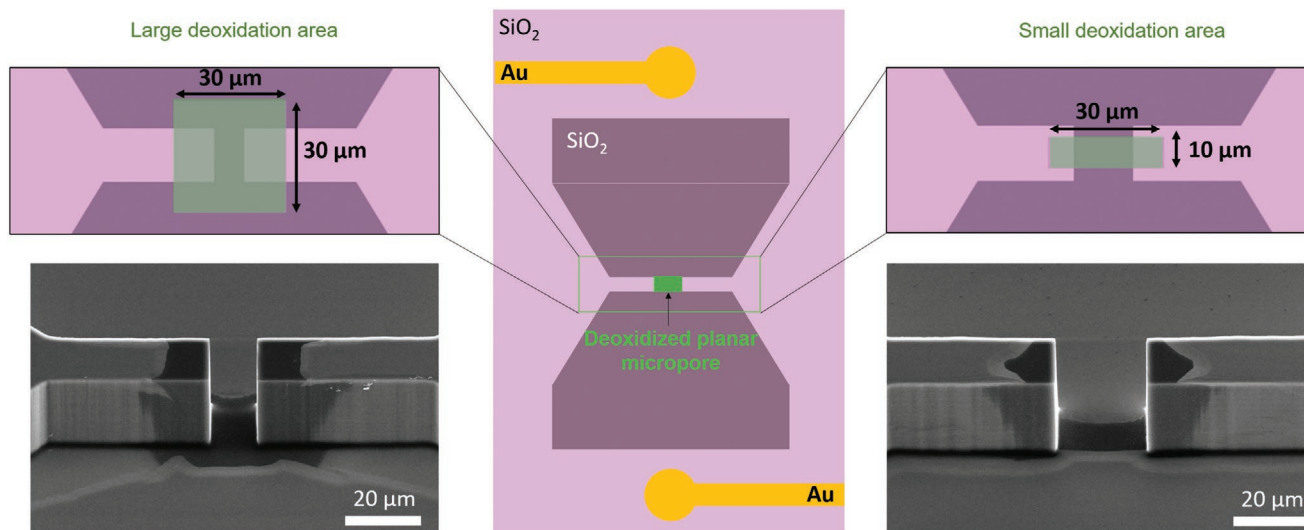


**Figure 2.** Designs of the chips used for the regioselective functionalization of planar micropores. The micropore was deoxidized according to two deoxidation patterns: a large  $30\ \mu\text{m} \times 30\ \mu\text{m}$  deoxidation around a  $20\ \mu\text{m} \times 10\ \mu\text{m}$  pore (scheme and SEM image on the left) and a small  $30\ \mu\text{m} \times 10\ \mu\text{m}$  deoxidation around a  $20\ \mu\text{m} \times 20\ \mu\text{m}$  pore (scheme and SEM image on the right).

deoxidation of silicon, the potential drop is mainly localized within the vicinity of the pore (within  $10\ \mu\text{m}$  of the pore center). When deoxidizing the pore, the repartition of the electric field changes with the location and size of the deoxidation pattern

(Figures 3B,4B). The “large” deoxidation leads to a concentration of the potential drop through the external pore walls which occurs both at the base of the pore (Figure 3B) and at its half-height (Figure 3C). In the case of the “small” deoxidation

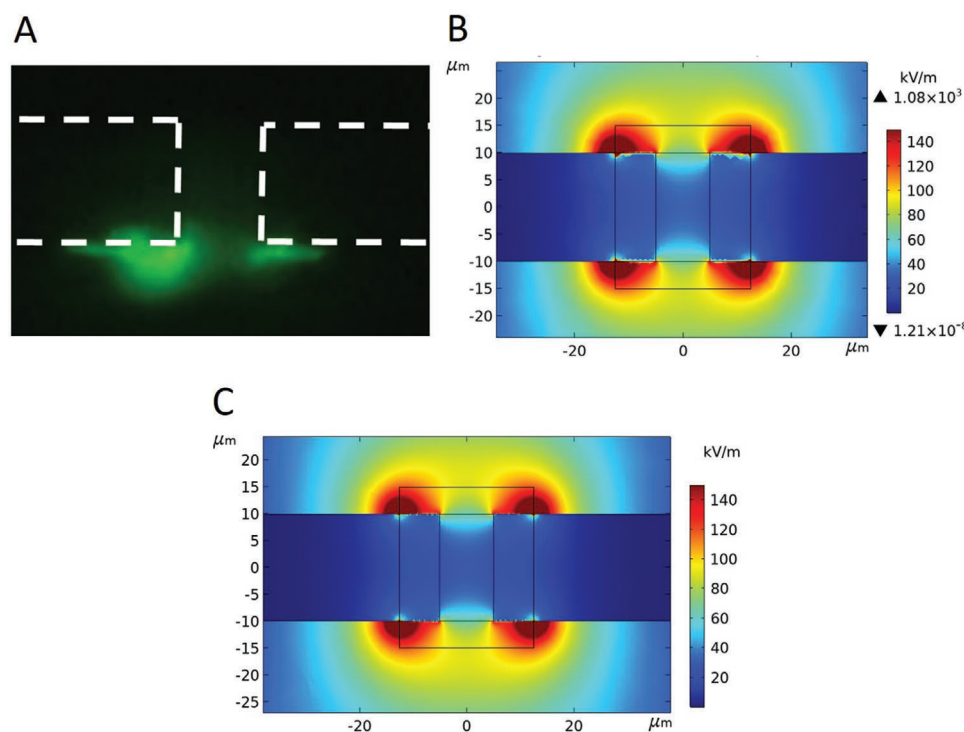


**Figure 3.** Electrodeposition of PPy in planar micropores in case of “large”  $30\ \mu\text{m} \times 30\ \mu\text{m}$  deoxidation. A) Revelation using fluorescence microscopy of polypyrrole-DNA depositions.  $10\ \text{V}$  for  $1\ \text{s}$  were applied between the two feeder Au electrodes. The electrodeposition solution was pyrrole  $100\ \text{mM}$  + py-ODN  $10\ \mu\text{M}$  + KCl  $10\ \text{mM}$ . Hybridization with biotinylated complementary strand was revealed using SAPE at  $575\ \text{nm}$  wavelength. Obj  $40\times$ , exposure time  $0.32\ \text{s}$ , binning  $4\times$ . Numerical simulations of the  $0\ \text{Hz}$  electric field norm ( $\text{V m}^{-1}$ ) distributions on the bottom B) and at mid-height C) of the planar micropore ( $20\ \mu\text{m} \times 10\ \mu\text{m}$ ) with “large”  $30\ \mu\text{m} \times 30\ \mu\text{m}$  deoxidation pattern, after application of  $10\ \text{V}$  between the feeder electrodes.

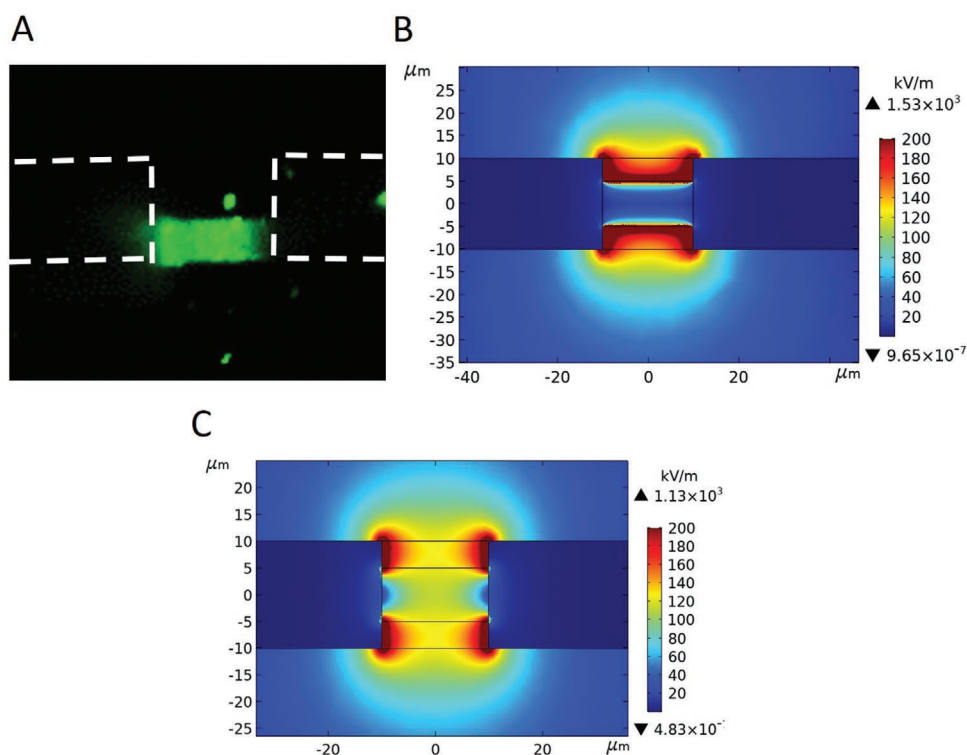


**Figure 4.** A) Electrodeposition of PPy in planar micropores in case of “small”  $10\ \mu\text{m} \times 30\ \mu\text{m}$  deoxidation. Revelation using fluorescence microscopy of polypyrrole-DNA depositions. 10 V for 1 s were applied between the two feeder Au electrodes. The electrodeposition solution was pyrrole 100 mM + pyrrole-ODN  $10\ \mu\text{M}$  + KCl 10 mM. Hybridization with biotinylated complementary strand was revealed using SAPE at wavelength. Obj 40 $\times$ , exposure time 1 s, binning 4 $\times$ . Numerical simulations of the 0 Hz electric field norm ( $\text{V m}^{-1}$ ) distributions on the bottom B) and at mid-height C) of the planar micropore ( $20\ \mu\text{m} \times 20\ \mu\text{m}$ ) with “small”  $30\ \mu\text{m} \times 10\ \mu\text{m}$  deoxidation pattern, after application of 10 V between the feeder electrodes.

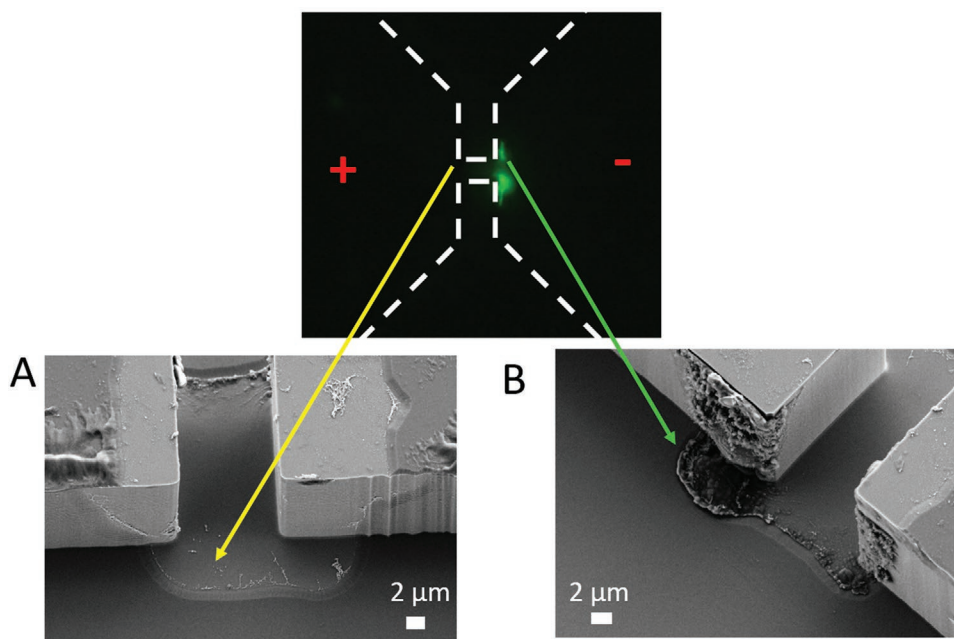


**Figure 5.** A) Fluorescence and B,C) SEM images of PPy functionalized large deoxidation pore from the compartment toward the B) positive feeder electrode and C) negative feeder electrode. The PPy film is clearly shown to be deposited on the deoxidized silicon walls and ground facing the negative feeder electrode. There is asymmetry in the deposition reflecting the asymmetry in the deoxydation. The amount of the PPy electrodeposited is reflected by the place and amount of the potential drop that is controlled by the geometry of the channel and the deoxydation pattern of the silicon micropore. Parameters of SEM: working distance 9.5 mm, acceleration voltage: 5 kV, SE2 mode magnification 2.76 k $\times$ .



**Figure 6.** Fluorescent microscopy of PPy-ODN functionalized micropore ( $10 \times 20 \mu\text{m}^2$ ) of large deoxidation ( $30 \times 30 \mu\text{m}^2$ ) after successive hybridization with A,C) complementary and B) non-complementary biotinylated DNA probes and further SAPE reaction. Between the different hybridizations, the chip was incubated in hot water for 15 min in order to regenerate, dehybridize, and regenerate the chip. Obj 40 $\times$ , exposure time 0.32 s, binning 4 $\times$ . Working electrode on left. 10 V for 1s using Py 100 mM + PPy-ODN + KCl 10 mM.

pattern, the highest electric potential norm is located simultaneously on the edges of the area of deoxidation across the entire pore on the one hand (Figure 4C), and at the base of the pore on the other hand (Figure 4B). The concentration of the voltage drop inside the pore increases while the area of the deoxidation of silicon decreases. These results are in perfect correlation with the experimental results we obtained above for pore functionalization, both by fluorescence and SEM microscopy. A deoxidation that protrudes from the micropore leads to a polarization of the outer walls of the pore while a deoxidation exclusively inside the micropore leads to a polarization of the inner surface at the base of the micropore. Figures S8 and S9, Supporting Information, show the commensurate evolution of this phenomenon with the size of the deoxidation area.

We recently published work demonstrating the confinement of ECL in micropores within similar devices. We attributed the phenomenon which takes place in the deoxidized silicon micropores to BPE.<sup>[36,41]</sup> We confirm here that the deoxidized part of the micropore polarizes under the application of a voltage between the feeder electrodes, but in addition we show that this polarization depends greatly on the configuration of the deoxidation area. In the deoxidized area, one part of the silicon acts as the positive pole and the other part as the negative pole.

For large deoxidation patterns, a region on one side of the pore wall forms a cathode, while forming an anode on the other side. For small deoxidation patterns, the micropore is split into two areas corresponding to anode and cathode. This is clearly a BPE process. Oxidation of pyrrole to PPy will take place at the positive pole while reduction of water to hydrogen will occur at the negative pole.

The possibility to tune the functionalization capabilities by varying the design of the deoxidation areas opens up the possibility of an easily implemented and standardized electrochemical technique for the functionalization of micropores and restrictions in microfluidic channels. The CLEF process should be adaptable to smaller pores down to nanometric size.

### 2.3. Toward Biosensing Capabilities

A surface functionalization technique for biosensors requires high robustness and should not lose recognition capabilities. We assessed the reusability and the specificity of the hybridization of ADN on the functionalized pores by successive hybridizations with complementary and non-complementary

probes. Hot water denaturation of the two DNA double strands was carried out in between each hybridization. The results show a strong and reproducible fluorescence response for complementary hybridization (Figure 6A,C). After each denaturation, the fluorescence signal disappears. A negligible response was obtained for the non-complementary hybridization, thus demonstrating the selectivity and the specificity of these assays (Figure 6B). Indeed, these results confirm the stability of the electrodeposited polymer for several hours under agitation and fluidic flow. The functionalization was reproducible and the film was stable when stored dried for six months. The CLEF technique should allow the functionalization of micropores with any kind of biomolecules, since conjugates of pyrrole with proteins, antibodies, or sugars can be easily synthesized. As the experimental conditions are mild, the conformation and activity of probes such as proteins are not affected.

### 3. Conclusion

In this work, we demonstrate a new functionalization technique of planar micropores, that is, micrometric restrictions in microfluidic channels made of silicon and silicon oxide. This contactless electrochemical functionalization technique is inspired by BPE and leads to highly localized functionalization of micropores. We benefit from the microfluidic spatial configuration to confine the potential drop to the immediate vicinity of the micropore, which allowed us to work at voltages two orders of magnitude lower than in the absence of the micropore. That is a considerable advantage, which is essential to keep the activity of the grafted biomolecules to within the micropore. The localization of the deposition can be tuned by the localization of the silicon oxide deoxidation and was predicted and validated thanks to numerical simulations of electric fields on the chip. We anticipate that this new functionalization technique will be of great interest for the conception of biosensors, especially in the case of multiplexed sensors where having different functional groups is a necessity. Indeed, this functionalization process is thought to be easily transferable to planar nanopores. The electric control of the potential drop through the targeted planar pore would make this multiplexing feasible. Preliminary results show the robustness of the biomolecule immobilization process and specific hybridization assays confirmed the biomolecule integrity and functionality.

## 4. Experimental Section

**Chemicals:** SU-8 2075 resin was purchased from Microchem (Westborough, MA). All other chemicals were obtained from Sigma-Aldrich (France). SYLGARD Kit 184 of silicon elastomer and curing agent were obtained from Dow Corning GmbH (Germany). The Streptavidin-R-Phycoerythrin conjugate (SAPE, 1 mg mL<sup>-1</sup>) was supplied by Invitrogen (France). Complementary and non-complementary biotinylated oligonucleotides (cODN-biot and ncODN-biot) and oligonucleotide probes for pyrrole-oligonucleotide conjugate synthesis were purchased from Eurogentec (France). Deionized water (18 M $\Omega$ .cm) was obtained with a Milli-Q water system (ELGA Purelab flex). Stock solutions (1 M) of Pyrrole (Py) were prepared by aliquoting pure pyrrole (from Interchim, France) in acetonitrile (Acros organics, France) and stored at -20 °C. N-hydroxysuccinimidyl 6-(pyrrol-yl)-caproate (NHS-pyrrole) was prepared as described by Grosjean et al.<sup>[37]</sup> Pyrrole-ODN (Py-ODN) conjugates were synthesized following the protocol described by Livache et al.<sup>[38]</sup> DNA sequences used in this work were designed to avoid the generation of any secondary structure.

- Sequence of pyrrole-oligonucleotide: Py-ODN: pyrrole-(T)10<sup>-5</sup>TGC GAT CGC AGC GGT AAC CTG ACC<sup>3</sup>
- Sequence of complementary biotinylated oligonucleotide: Biotin-<sup>5</sup>GGT CAG GTT ACC GCT GCG ATC GCA<sup>3</sup>
- Sequence of non-complementary biotinylated oligonucleotide: Biotin-<sup>5</sup>GGT CTA CCT ACC CGC ACG ATG GTC<sup>3</sup>

**Buffers and Electrolytes Composition:** Hybridization buffer (HB): 0.02 M sodium phosphate buffer, 1.1 M NaCl, 5.4 mM KCl, 4% v/v 50 $\times$  Denhardt, 0.2% v/v salmon sperm DNA, 0.3% v/v Tween 20, pH = 7.4.

Washing buffer (WB): 0.01 M sodium phosphate buffer, 0.55 M NaCl, 2.7 mM KCl, 0.15% v/v Tween 20, pH = 7.4.

Electrodeposition electrolyte: KNO<sub>3</sub> 10 mM, KCl 10 mM

**Fabrication of Silicon Chips Integrating Planar Micropores:** The planar micropores were fabricated using top-down micromachining of 100 mm *p*-type silicon substrates (resistivity  $\rho < 0.01 \Omega$ .cm) as described elsewhere.<sup>[36]</sup> The fabrication process illustrated in Figure S1, Supporting Information, starts by transferring the micropore patterns into the silicon wafers by a photolithography step using the positive photoresist ECI 3012 (2.5  $\mu$ m-thick) followed by reactive ion etching (by means of an inductively coupled plasma source manufactured by Alcatel Comptech

Inc with 250 sccm SF<sub>6</sub>, 250 sccm C<sub>4</sub>F<sub>8</sub>, 35 sccm O<sub>2</sub>). Following the etching step, the residual ECI layer was removed by acetone and plasma O<sub>2</sub> (800 W, 5 min). Then, dry oxidation of the silicon wafers was performed by thermally growing 300 nm of SiO<sub>2</sub> in a dedicated furnace. Deoxidation of the micropores following two distinct patterns (either the internal part or the entire surface of the pore, indicated as small or large patterns in Figure 2) was then achieved following a two-step process combining photolithography (with positive photoresist AZ 4999, 8  $\mu$ m-thick, deposited with a Suss Microtec automatic spray-coating system) and wet etching in buffered oxide etchant (7:1) for 4 min. The residual AZ 4999 layer was removed by acetone and O<sub>2</sub> plasma. Finally, metal electrodes consisting of 50 nm/200 nm-thick Ti/Au layers deposited by physical vapour deposition (Univex 450C) were patterned on the oxidized silicon by photolithography (photoresist AZ 4999) and wet etching in appropriate baths. The wafers were then diced into 20 mm  $\times$  20 mm chips containing a single micropore.

In order to prepare the PDMS channels to cap the micropores (Figure S3b, Supporting Information), SU-8 on silicon moulds were fabricated by laser photolithography. SU-8 2075 negative photoresist was spin coated (5 s at 500 rpm/30 s at 2000 rpm/5 s at 500 rpm with 300 rpm s<sup>-1</sup> acceleration) onto previously sonicated (5 min in acetone then in isopropanol) and dried (180 °C for 15 min) 100 mm silicon wafer. The SU-8 layer underwent baking at 65 °C for 5 min then 95 °C for 20 min and 65 °C for 5 min. The design of the channels was directly written on the resist via laser photolithography (70 mW, 70%,  $\mu$ PG 101 Heidelberg Instrument, Germany) followed by a post exposure bake (65 °C for 2 min then 95 °C for 8 min). The SU-8 patterns were developed for 10 min in dedicated developer and for 30 s in IPA. The samples were finally hard baked at 150 °C for 15 min and the height of the pattern were measured to be 140  $\mu$ m using a profilometer (Dektak DXT "E", Milpitas, CA).

Finally, the PDMS channels were obtained by pouring a mixture of elastomer and curing agent at a ratio of 10:1 in weight over the SU-8 mould. Degassing of the PDMS mixture was carried out before and after the moulding step by means of a vacuum pump. PDMS was cured at 60 °C for 1 h before demoulding. The prepared PDMS and the silicon chips were then activated using ICP plasma (Plasmalab100 from oxford, UK/ 80 mTorr/10 sccm O<sub>2</sub>/100 W RF power/150 W ICP power/5 min/20 °C). After plasma activation, the silicon chip and the PDMS slab were aligned using MJB4 (Suss MicroTec, Germany) and brought into contact to create a sealed channel allowing liquid to

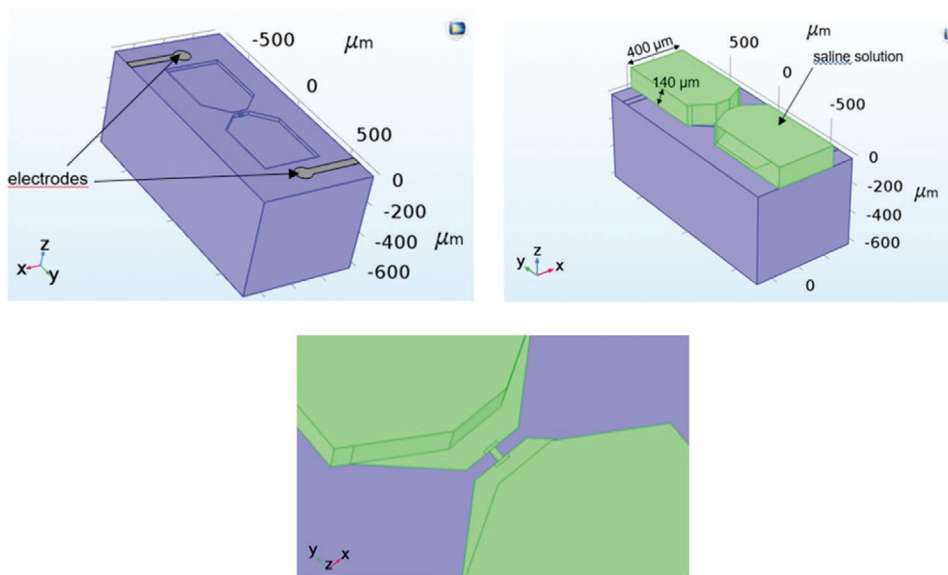


**Figure 7.** BPE chip geometry. Upper left: silicon chip (blue) and feeder Au electrodes (grey). Upper right: saline solution (green). Lower: top view on the planar pore restriction.

**Table 1.** Electric properties of the materials present in the chip.

	Electric conductivity $\sigma$ [ $S\ m^{-1}$ ]	Dielectric constant $\epsilon_r$
p-doped Si	7.1	11
SiO <sub>2</sub>	10 <sup>-14</sup>	4.5
Saline solution (bulk)	1.39	78.5 (water)
Au	45.10 <sup>6</sup>	1

flow inside the micropore as described by Cottet et al.<sup>[39]</sup> (Figure S3, Supporting Information).

**CLEF:** An electrolyte solution (0.5 M KNO<sub>3</sub>, 10 mM KCl) containing pyrrole (100 mM) and pyrrole-ODN conjugate (3.5 μM) was injected within the two compartments separated by a micropore using the fluidic inlet made in the PDMS slab. The silicon microchip was mounted on a custom-made printed circuit board (PCB) in order to electrically couple the electrodes on the chip to the potentiostat. The chip was held by a 3D-printed holder for optimal alignment between the electrodes and the connectors on the PCB. A two-electrode system was used to apply a voltage pulse of 10 V for 1 s using a Biologic SP-300 potentiostat. The electrodes were deposited on the insulating SiO<sub>2</sub> layer at a fixed predetermined position. The chronoamperograms were systematically recorded to allow for process optimization and validation of the reproducibility. The optimal deposition conditions (voltage, duration) were found to be 10 V and 1 s. The chip was then washed by circulating deionized water within the chip through the PDMS microfluidic inlets. The PDMS was then removed in order to continue the study by microscope observation and fluorescence detection. All the experiments were reproduced at least three times.

**Fluorescence Detection:** After electrodeposition of polypyrrole coupled with oligonucleotides, HB was left on the chip for 5 min to saturate the surface and limit non-specific adsorption. The complementary or non-complementary biotinylated oligonucleotide (2% v/v diluted in HB), for a positive or negative control, respectively, was then brought into contact with the chip. The chip was incubated at 40 °C for 15 min in a humid chamber to allow hybridization. The chip was then washed with WB and incubated with streptavidin-R-phycoerythrin (5% v/v diluted in WB) for 5 min in the dark at room temperature. After washing the chip again with WB, the fluorescence emission was measured at 575 nm with a fluorescence microscope (Olympus BX 60) equipped with a CCD camera (ORCA-Flash 4.0 C11440, Hamamatsu) controlled by the HCLImageLive software. After fluorescence observation, regeneration of ODN arrays was carried out using hot, deionized water (60 °C) for 5 min to allow denaturation of the ODN double-strands.

**Scanning Electron Microscopy:** The SEM images were obtained with a FEI Helios 600i SEM instruments (Plateforme technologique amount, CEA Grenoble).

**Numerical Simulations:** To investigate the BPE behavior at the micropore level, a complete numerical model was set up in the Finite Element analysis software Comsol Multiphysics, based on the Complex Electrokinetic Equation 1, derived from the Maxwell's equations under the quasi-static assumption (ACDC module).<sup>[40]</sup> As voltage pulses of 10 V for 1 s were applied to the feeder electrodes during the BPE process, the temporal potential  $V(t)$  is transformed using the complex formalism  $V(t) = V_0^* e^{j\omega t}$ , where  $V_0^*$  is the complex amplitude potential sinusoidal potentials of angular frequency  $\omega$  (rad s<sup>-1</sup>):

$$\vec{\nabla} \cdot (-\sigma^* \vec{\nabla} V_0^*) = 0 \quad (1)$$

where  $\sigma^* = \sigma + i\omega\epsilon$  is the frequency-dependent complex conductivity,  $\sigma$  being the conductivity ( $S\ m^{-1}$ ), and  $\epsilon$  the permittivity ( $F\ m^{-1}$ ).

Numerical simulations have taken into account the complete geometry of the microfluidic chip (Figure 7). The electric parameters of the constitutive materials of the chip are given in Table 1.

The objectives of the numerical simulations being limited to the evaluation of the effect of the geometrical restriction on the electric field amplitude, in a first simplifying approach the BPE chip was subjected

to a sinusoidal voltage of amplitude 10 V (between -5 and +5 V) at a frequency varying between 0 and 10 Hz. To be consistent with the experimental data, the simulations presented in the manuscript were carried out at 0 Hz. The electrochemical double layer theoretically formed at the feeder Au electrode surfaces was neglected.<sup>[40]</sup>

## Supporting Information

Supporting Information is available from the Wiley Online Library or from the author.

## Acknowledgements

The authors thank the Agence Nationale de la Recherche (Planarpore ANR-15-CE18-0027). This work has been partially supported by Labex ARCANE and CBH-EUR-GS (ANR-17-EURE-0003). SyMMES laboratory is part of Labex LANEF program (ANR-10-LABX-51-01). This work was supported by the LAAS-CNRS technology platform, a member of the Renatech network. Larry O'Connell is acknowledged for fruitful proofreading.

## Conflict of Interest

The authors declare no conflict of interest.

## Data Availability Statement

Research data are not shared.

## Keywords

biosensor, electrofunctionalization, localized functionalization, numerical simulations, planar pore

Received: November 26, 2020

Revised: January 14, 2021

Published online:

- [1] S. Howorka, *Nat. Nanotechnol.* **2017**, *12*, 619.
- [2] M. Tsutsui, T. Yoshida, K. Yokota, H. Yasaki, T. Yasui, A. Arima, W. Tonomura, K. Nagashima, T. Yanagida, N. Kaji, M. Taniguchi, T. Washio, Y. Baba, T. Kawai, *Sci. Rep.* **2017**, *7*, 17371.
- [3] J. Ryu, W. Choi, E.-S. Jeon, C.-W. Song, C.-S. Han, *Sens. Actuators, B* **2019**, *288*, 454.
- [4] A. T. Carlsen, O. K. Zahid, J. Ruzicka, E. W. Taylor, A. R. Hall, *ACS Nano* **2014**, *8*, 4754.
- [5] M. Lepoitevin, T. Ma, M. Bechelany, J.-M. Janot, S. Balme, *Adv. Colloid Interface Sci.* **2017**, *250*, 195.
- [6] S. M. Iqbal, D. Akin, R. Bashir, *Nat. Nanotechnol.* **2007**, *2*, 243.
- [7] M. Wanunu, A. Meller, *Nano Lett.* **2007**, *7*, 1580.
- [8] A. Tufani, G. O. Ince, *J. Membr. Sci.* **2019**, *575*, 126.
- [9] J. C. Whelan, B. I. Karawdeniya, Y. M. N. D. Y. Bandara, B. D. Velleco, C. M. Masterson, J. R. Dwyer, *ACS Appl. Mater. Interfaces* **2014**, *6*, 10952.
- [10] H. Wang, M. Wei, Z. Zhong, Y. Wang, *J. Membr. Sci.* **2017**, *535*, 56.
- [11] B. Yameen, M. Ali, R. Neumann, W. Ensinger, W. Knoll, O. Azzaroni, *Small* **2009**, *5*, 1287.
- [12] N. Reber, A. Küchel, R. Spohr, A. Wolf, M. Yoshida, *J. Membr. Sci.* **2001**, *193*, 49.

- [13] X. Hou, W. Guo, F. Xia, F.-Q. Nie, H. Dong, Y. Tian, L. Wen, L. Wang, L. Cao, Y. Yang, J. Xue, Y. Song, Y. Wang, D. Liu, L. Jiang, *J. Am. Chem. Soc.* **2009**, *131*, 7800.
- [14] B. N. Miles, A. P. Ivanov, K. A. Wilson, F. Doğan, D. Japrun, J. B. Edel, *Chem. Soc. Rev.* **2013**, *42*, 15.
- [15] J. Nilsson, J. R. I. Lee, T. V. Ratto, S. E. Létant, *Adv. Mater.* **2006**, *18*, 427.
- [16] A. Bouchet, E. Descamps, P. Mailley, T. Livache, F. Chatelain, V. Haguët, *Small* **2009**, *5*, 2297.
- [17] J. Liu, P. Pham, V. Haguët, F. Sauter-Starace, L. Leroy, A. Roget, E. Descamps, A. Bouchet, A. Buhot, P. Mailley, T. Livache, *Anal. Chem.* **2012**, *84*, 3254.
- [18] J. Liu, C. Hébert, P. Pham, F. Sauter-Starace, V. Haguët, T. Livache, P. Mailley, *Small* **2012**, *8*, 1345.
- [19] J. Liu, R. Bombera, L. Leroy, Y. Roupioz, D. R. Baganizi, P. N. Marche, V. Haguët, P. Mailley, T. Livache, *PLoS One* **2013**, *8*, e57717.
- [20] A. Bouchet-Spinelli, E. Descamps, J. Liu, A. Ismail, P. Pham, F. Chatelain, T. Leïchlé, L. Leroy, P. N. Marche, C. Raillon, A. Roget, Y. Roupioz, N. Sojic, A. Buhot, V. Haguët, T. Livache, P. Mailley, *Biosensors* **2019**, *9*, 121.
- [21] M. R. Maurya, V. Toutam, P. Singh, S. Bathula, *Mater. Sci. Semicond. Process.* **2019**, *100*, 140.
- [22] J. Vacik, V. Hnatowicz, V. Havranek, D. Fink, P. Apel, P. Horak, G. Ceccio, A. Cannavo, A. Torrisi, *Radiat. Eff. Defects Solids* **2019**, *174*, 148.
- [23] J. Li, D. Stein, C. McMullan, D. Branton, M. J. Aziz, J. A. Golovchenko, *Nature* **2001**, *412*, 166.
- [24] S. M. Gilbert, S. Liu, G. Schumm, A. Zettl, *MRS Adv.* **2018**, *3*, 327.
- [25] K. Briggs, M. Charron, H. Kwok, T. Le, S. Chahal, J. Bustamante, M. Waugh, V. Tabard-Cossa, *Nanotechnology* **2015**, *26*, 084004.
- [26] N. Ahmed, S. Darwish, A. M. Alahmari, *Mater. Manuf. Processes* **2016**, *31*, 1121.
- [27] T. Gilboa, A. Zrehen, A. Girsault, A. Meller, *Sci. Rep.* **2018**, *8*, 9765.
- [28] M. J. Kim, M. Wanunu, D. C. Bell, A. Meller, *Adv. Mater.* **2006**, *18*, 3149.
- [29] M. Islam, M. M. Bellah, A. Sajid, M. R. Hasan, Y. -t Kim, S. M. Iqbal, *Sci. Rep.* **2015**, 13031.
- [30] A. A. Adams, P. I. Okagbare, J. Feng, M. L. Hupert, D. Patterson, J. Göttert, R. L. McCarley, D. Nikitopoulos, M. C. Murphy, S. A. Soper, *J. Am. Chem. Soc.* **2008**, *130*, 8633.
- [31] H. Yasaki, T. Yasui, T. Yanagida, N. Kaji, M. Kanai, K. Nagashima, T. Kawai, Y. Baba, *J. Am. Chem. Soc.* **2017**, *139*, 14137.
- [32] J. Guo, T. S. Pui, Y.-L. Ban, A. R. A. Rahman, Y. Kang, *IEEE Trans. Biomed. Eng.* **2013**, *60*, 3269.
- [33] Y. Nakajima, T. Ukai, T. Shimizu, K. Ogata, S. Iwai, N. Takahashi, A. Aki, T. Mizuki, T. Maekawa, T. Hanajiri, *Anal. Chem.* **2017**, *89*, 12450.
- [34] N. Takahashi, A. Aki, T. Ukai, Y. Nakajima, T. Maekawa, T. Hanajiri, *Sens. Actuators, B* **2011**, *151*, 410.
- [35] C. Raillon, P. Cousin, F. Traversi, E. Garcia-Cordero, N. Hernandez, A. Radenovic, *Nano Lett.* **2012**, *12*, 1157.
- [36] A. Ismail, S. Voci, P. Pham, L. Leroy, A. Maziz, L. Descamps, A. Kuhn, P. Mailley, T. Livache, A. Buhot, T. Leïchlé, A. Bouchet-Spinelli, N. Sojic, *Anal. Chem.* **2019**, *91*, 8900.
- [37] L. Grosjean, B. Cherif, E. Mercey, A. Roget, Y. Levy, P. N. Marche, M.-B. Villiers, T. Livache, *Anal. Biochem.* **2005**, *347*, 193.
- [38] T. Livache, B. Fouque, A. Roget, J. Marchand, G. Bidan, R. Téoule, G. Mathis, *Anal. Biochem.* **1998**, *255*, 188.
- [39] J. Cottet, C. Vaillier, F. Buret, M. Frénéa-Robin, P. Renaud, *Biomicrofluidics* **2017**, *11*, 064111.
- [40] P. Pham, S. Roux, F. Matonti, F. Dupont, V. Agache, F. Chavane, *J. Neural Eng.* **2013**, *10*, 046002.
- [41] S. Voci, A. Ismail, P. Pham, J. Yu, A. Maziz, F. Mesnilgrete, L. Reynaud, T. Livache, P. Mailley, A. Buhot, T. Leichle, A. Kuhn, L. Leroy, A. Bouchet-Spinelli, N. Sojic, *J. Electrochem. Soc.* **2020**, *167*, 137509.